ELSEVIER

Volume 182, Number 10, October 2009

JOURNAL OF SOLID STATE CHEMISTRY

www.elsevier.com/locate/jssc

CONTENTS

Abstracted/indexed in BioEngineering Abstracts, Chemical Abstracts, Coal Abstracts, Current Contents/Physics, Chemical, & Earth Sciences, Engineering Index, Research Alert, SCISEARCH, Science Abstracts, and Science Citation Index. Also covered in the abstract and citation database SCOPUS®. Full text available on ScienceDirect®.

Regular Articles

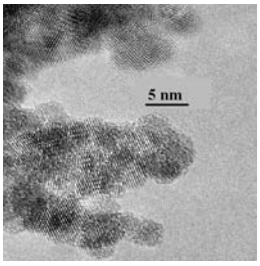

High-resolution transmission electron microscopy (HRTEM) observation of UO2+x powders obtained at a pH = 6.5.

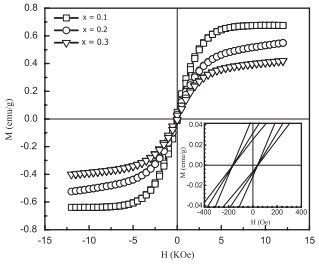

Figure shows the magnetization data of $Zn_{1-x}Co_xS$ ($0.1 \le x \le 0.3$) nanoparticles annealed at 573 K/2 h in vacuum and measured at 300 K. This interesting feature of systematic reduction in magnetization may be due to introduction of antiferromagnetic ordering with increasing 'Co' concentration which may be due to competition between the antiferromagnetic and ferromagnetic ordering within the sample. One could also observe the exchange bias effect which is an interface interaction observed in a ferromagnetic–antiferromagnetic mixture. The exchange bias field (loop shift) towards negative field was around 63 Oe for the $Zn_{1-x}Co_xS$ ($0.1 \le x \le 0.3$) nanoparticles.

Regular Articles—Continued

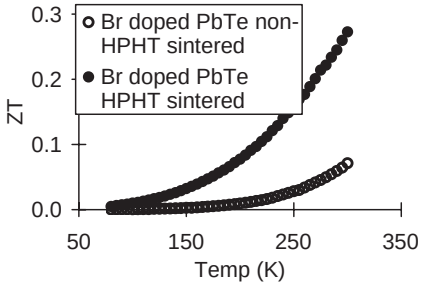

The effect, on thermoelectric properties, of sintering undoped and Br doped PbTe at pressures $\geq$4.0 GPa and 1045 °C are reported and compared with conventionally sintered materials.

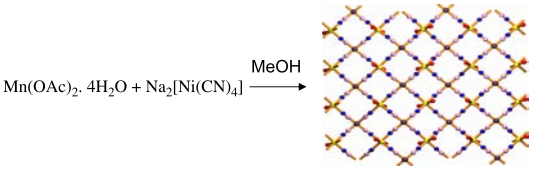

A coordination polymer, $\{Mn(H_2O)_2[NiCN]_4 \cdot 4H_2O\}_n$, showed that the coordination layers are stacked on top of each other sandwiching 2D ice layer of boat-shaped hexagonal water clusters.

Continued

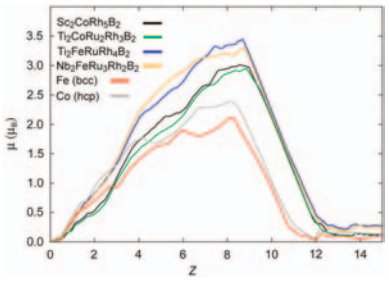

Theoretically determined (spin-polarized LMTO-GGA) local magnetic moments as a function of the chemical valence Z for various intermetallic borides.

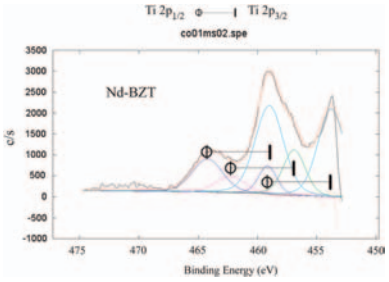

XPS narrow-scan spectra of Ti 2*p* doublets of the Nd-doped BZT films deposited on Pt-coated Si substrate.

A powder neutron diffraction study suggests that the relaxor ferroelectric $Pb_2Bi_4Ti_5O_{18}$ undergoes the phase transition sequence *F*2*mm*–*I*4*mm*–*I*4/*mmm* with increasing temperature.

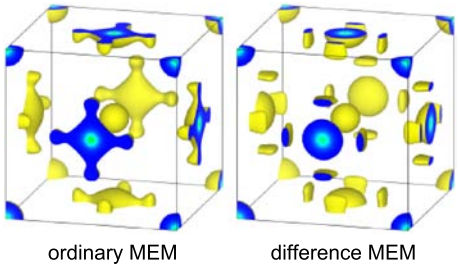

A novel method, difference maximum entropy method (MEM) analysis of the neutron diffraction data, is proposed for revealing the detailed structure around hydrogen atoms in proton-conducting oxides. This MEM analysis uses the differences between the structure factors of protium- and deuterium-dissolved crystals and improves the spatial resolution of the MEM mapping around the hydrogen atoms.

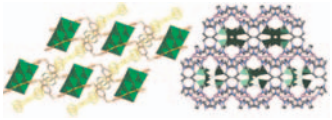

Two new examples of Ag/organonitrogen/polyoxovanadate composite solids with rare poly(pseudo-rotaxane) architectures have been synthesized and characterized.

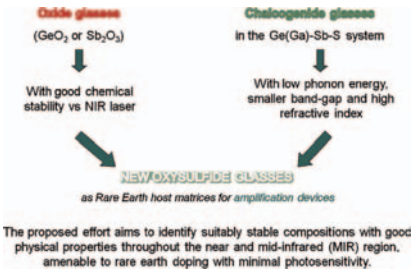

In this paper, we demonstrate the successful processing of active rare earth doped oxysulfide glasses by melting the chalcogenide glass with Er_2O_3 and Sb_2O_3 but also by melting the Er^{3+} doped chalcogenide glass with Sb_2O_3. These new glasses were found to be photo-sensitive to near-IR femtosecond laser irradiation and to exhibit a surface photo-expansion after laser irradiation which remains, as expected, lower than similar response seen for oxygen-free chalcogenide glasses.

Crystal structures and high-temperature phase transitions of the new ordered double perovskites Sr_2SmSbO_6 and Sr_2LaSbO_6

A. Faik, E. Iturbe-Zabalo, I. Urcelay and J.M. Igartua

Page 2656

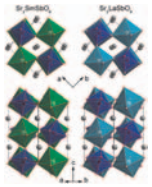

Clinographic projections of the structures of the new ordered double perovskites (a) Sr_2SmSbO_6 and (b) Sr_2LaSbO_6, along the $[001]_p$ and $[010]_p$ directions, as indicated, in the upper and in the lower panels, respectively. SmO_6 octahedra are shown green, LaO_6 in cyan, SbO_6 in blue and Sr cations in gray. Sr_2LaSbO_6 is more distorted than Sr_2SmSbO_6, as can be appreciated in the upper panel in the projection of the cuboctahedral site occupied by the Sr. The angle of rotation of the octahedra around the simple perovskite cubic axis is greater in the more distorted Sr_2LaSbO_6 phase.

First-principles studies of Al–Ni intermetallic compounds

Dongmin Shi, Bin Wen, Roderick Melnik, Shan Yao and Tingju Li

Page 2664

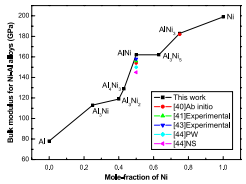

Calculated bulk modulus compared to experimental and other theoretical values for the Al–Ni intermetallic compounds.

Graphitic carbon nitride $C_6N_9H_3 \cdot HCl$: Characterisation by UV and near-IR FT Raman spectroscopy

Paul F. McMillan, Victoria Lees, Eric Quirico, Gilles Montagnac, Andrea Sella, Bruno Reynard, Patrick Simon, Edward Bailey, Malek Deifallah and Furio Corà

Page 2670

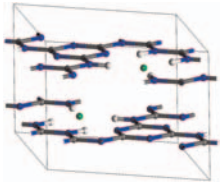

The graphitic layered compound $C_6N_9H_3 \cdot HCl$ was prepared by reaction between melamine and cyanuric chloride under high pressure–high temperature conditions in a piston cylinder apparatus and characterised using SEM, powder X-ray diffraction, UV Raman and near-IR Fourier transform Raman spectroscopy using near-IR excitation. Theoretical calculations using density functional methods permitted evaluation of the mode of attachment of H atoms to nitrogen sites around the $C_{12}N_{12}$ voids within the layered structure and also led to better understanding of the X-ray diffraction pattern. Sharp peaks in the UV Raman spectra are due to C_3N_3 triazine ring units in the structure, that may be enhanced by resonance Raman effects. Broadening in the UV and near-IR FT Raman spectra indicate possible disordering within the graphitic layers or electron–phonon coupling effects.

Electronic band structure of $CaUO_4$ from first principles

S.F. Matar and G. Demazeau

Page 2678

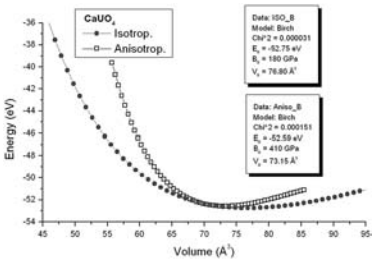

Energy versus volume variation for isotropic and anisotropic compressions within $CaUO_4$. Fit results with Birch EOS are given in inserts.

A simple solvothermal synthesis of MFe_2O_4 (M = Mn, Co and Ni) nanoparticles

S. Yáñez-Vilar, M. Sánchez-Andújar, C. Gómez-Aguirre, J. Mira, M.A. Señarís-Rodríguez and S. Castro-García

Page 2685

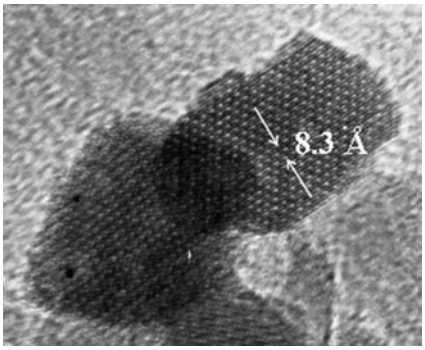

An adaptation of the solvothermal method allow us to obtain stable suspensions of monodispersed particles of MFe_2O_4 (M = Mn, Co and Ni), with diameters ranging from 5 to 10 nm, and with good crystallinity.

Large-scale synthesis, characterization and microwave absorption properties of carbon nanotubes of different helicities

Xiaosi Qi, Yi Yang, Wei Zhong, Yu Deng, Chaktong Au and Youwei Du

Page 2691

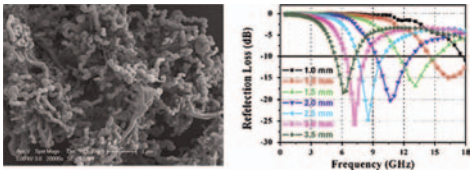

FESEM image of Sample B and reflection loss versus frequency of Composite B (containing 30 wt% of Sample B) in the range of 2–18 GHz.

Continued

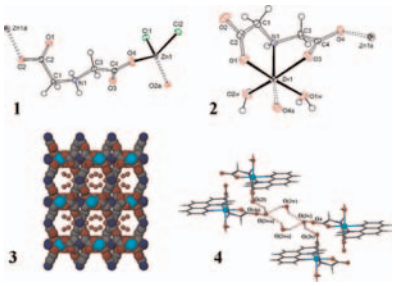

Reaction of zinc salt with iminodiacetic acid afforded three new coordination polymers **1**–**3** and a monomer **4**, which is dependent on pH value and molar ratio of the reactants.

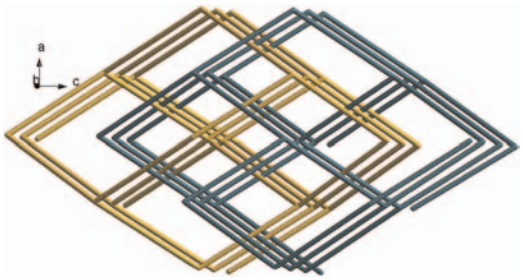

Five new transition metal coordination polymers based on flexible H_2tzda and bpe have been hydrothermally synthesized and characterized by X-ray diffraction, luminescent emission spectra and low-temperature magnetic measurements, respectively.

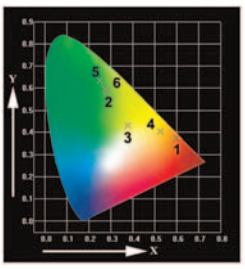

The advantages of core-shell phosphors are the easy availability of homogeneous spherical morphology in different size, and its corresponding luminescence color can change from red, yellow to green.

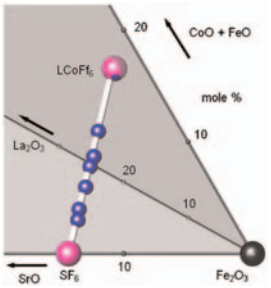

M-type hexaferrite solid solution series $Sr_{1-x}La_xFe^{2+}{}_{x-y}Co^{2+}{}_y Fe^{3+}{}_{12-x}O^{19}$ ($0 \le x \le 1$ and $0 \le y \le 0.40$) at 1300 °C; M-type contains significant amounts of FeO even at 1200 °C; blue = data from electronprobe microanalyses; $SF_6 = SrFe^{3+}_{12}O_{19}$; $LCoFf_6 = LaCo_{0.4}Fe^{2+}_{0.6}Fe^{3+}_{11}O_{19}$; S = SrO; L = La_2O_3; Co = CoO; F = Fe_2O_3; f = FeO.

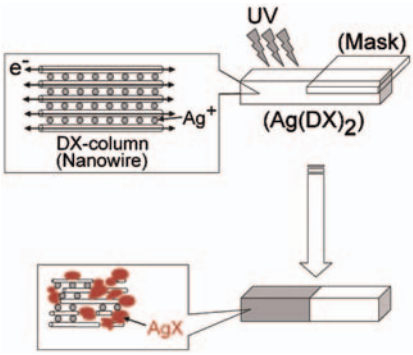

By UV irradiation with appropriate masks, a part of single crystal of organic conductors irreversibly turned diamagnetic retaining their original crystalline shapes.

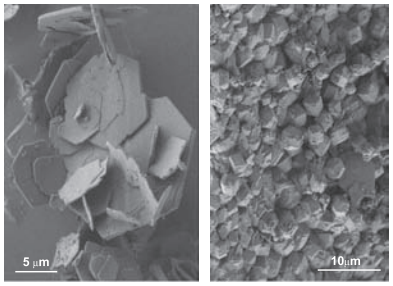

We use in-situ synchrotron diffraction to observe the decomposition of layer compound calcium monosulfoaluminate 14-hydrate (left) to form hydrogarnet (right)and β-anhydrite under hydrothermal conditions.

Displacive disorder and dielectric relaxation in the stoichiometric bismuth-containing pyrochlores, $Bi_2M^{III}NbO_7$ (M = In and Sc)

Yun Liu, Ray L. Withers, Hai Binh Nguyen, Kim Elliott, Qijun Ren and Zhanghai Chen

Page 2748

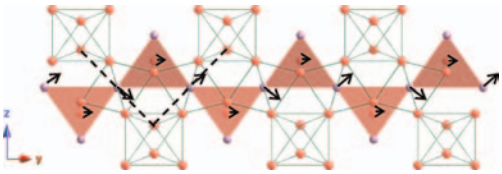

The characteristic 1-d, β-cristobalite type displacive disorder of the $O'Bi_2$ tetrahedral sub-structure responsible for the dipoles and glassy relaxation behaviour of the BIN and BSN, Bi-pyrochlores.

Compositional dependence of the nonlinear refractive index of new germanium-based chalcogenide glasses

L. Petit, N. Carlie, H. Chen, S. Gaylord, J. Massera, G. Boudebs, J. Hu, A. Agarwal, L. Kimerling and K. Richardson

Page 2756

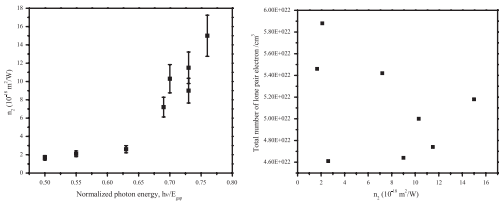

In this paper, we report results of n_2 measurements of new chalcogenide glasses in the Ge–Sb–S–Se system using a modified Z-Scan technique. n_2 is found to increase with an increase of normalized photon energy, regardless of chalcogen type, but does not depend on the concentration of lone pair electron.

Correlation between optical constants and crystal chemical parameters of ZrW_2O_8

Robert D. Shannon, Reinhard X. Fischer, Olaf Medenbach, Eric Bousquet and Philippe Ghosez

Page 2762

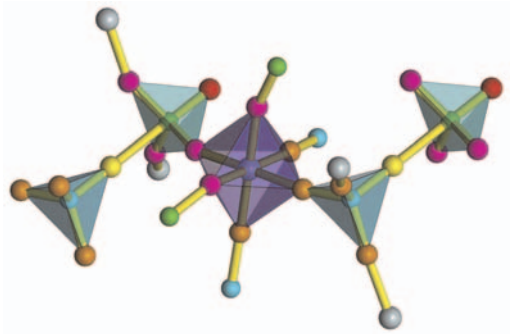

Refractive indices of ZrW_2O_8, measured at $\lambda = 435.8$–643.8 nm and a one-term Sellmeier equation allow the determination of n_D ($\lambda = 589.3$ nm) of 1.8794 and a dispersion value, A, of 114×10^{-16} m^2. The unusually large difference between the observed ZrW_2O_8 polarizability of 20.087 Å^3 and the calculated total polarizability α_T of 17.59 Å^3 ($\Delta = +12.4\%$) is attributed to (1) a large M–O–W angle, (2) a high degree of W $5d$–$O_{(terminal)}$ $2p$ and Zr nd–O $2p$ hybridization, and (3) unusually high oxygen displacement factors, B(O), normalized to B(W).

Lanthanide N,N′-piperazine-bis(methylenephosphonates) (Ln = La, Ce, Nd) that display flexible frameworks, reversible hydration and cation exchange

John P.S. Mowat, John A. Groves, Michael T. Wharmby, Stuart R. Miller, Yang Li, Philip Lightfoot and Paul A. Wright

Page 2769

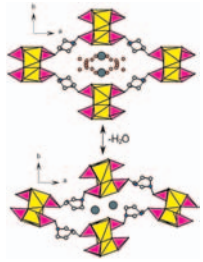

The lanthanides La, Ce and Nd give a family of metal organic frameworks based on N,N′-piperazinebismethylenephosphonate ligands: these display reversible dehydration, structural flexibility and cation exchange.

Magnetic nanoparticles for power absorption: Optimizing size, shape and magnetic properties

M.A. Gonzalez-Fernandez, T.E. Torres, M. Andrés-Vergés, R. Costo, P. de la Presa, C.J. Serna, M.P. Morales, C. Marquina, M.R. Ibarra and G.F. Goya

Page 2779

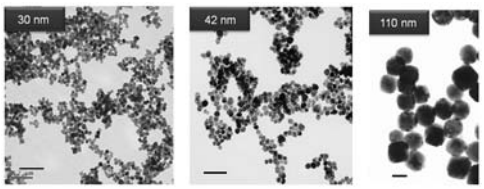

The magnetic properties of Fe_3O_4 nanoparticles from 5 to 110 nm are presented, and their efficiency as heating agents discussed as a function of particle size, shape and surface functionalization.

Synthesis and visible light photocatalysis of Fe-doped TiO_2 mesoporous layers deposited on hollow glass microbeads

Lifeng Cui, Yuansheng Wang, Mutong Niu, Guoxin Chen and Yao Cheng

Page 2785

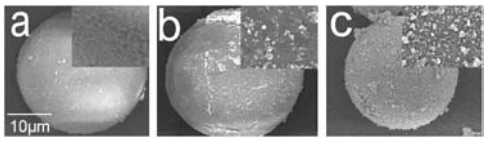

Nano-composite of Fe-doped anatase TiO_2 nanocrystals loaded on the hollow glass microbeads was prepared by co-thermal hydrolysis deposition. Photodegradation of the methyl orange was achieved under visible light irradiation, revealing the potential applicability of such nano-composite in some industry fields.

Continued

Rational synthetic strategy: From ZnO nanorods to ZnS nanotubes

Ran Yi, Guanzhou Qiu and Xiaohe Liu

Page 2791

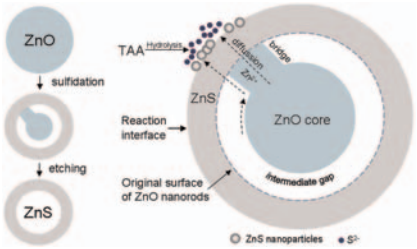

ZnS nanotubes can be successfully synthesized via a facile conversion process from ZnO nanorods precursors. The photoluminescence (PL) characterization shows much enhanced PL emission of tubular ZnO/ZnS core/shell nanocomposites.

Crystallization and second harmonic generation in potassium–sodium niobiosilicate glasses

Antonio Aronne, Esther Fanelli, Pasquale Pernice, Simone Peli, Claudio Giannetti and Gabriele Ferrini

Page 2796

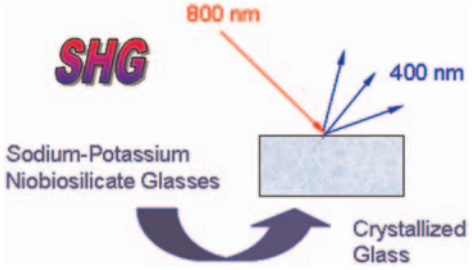

Synthesis of glasses $(23-x)K_2O \cdot xNa_2O \cdot 27Nb_2O_5 \cdot 50SiO_2$ (x=0, 5, 10, 15 and 23) from which SHG active phases crystallize by bulk nucleation for non-linear optical nanostructured glasses.

In-situ oxidation of block copolymer for producing copper oxalate or copper oxide nanowires in mesoporous channels

Jiang Li, AiGuo Kong, WenJuan Wang, XinHua Zhao, Fan Yang and YongKui Shan

Page 2801

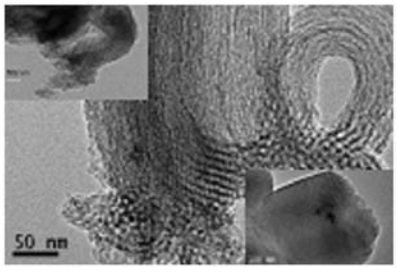

Copper oxalate or copper oxide nanowires embedded in the nanoscale channels of mesoporous SBA-15 are created by in-situ oxidation of block polymer template materials, which show the good electrochemical hydrogen storage ability.

Compositional control of electrical transport properties in the new series of defect thiospinels, $Ga_{1-x}Ge_xV_4S_{8-\delta}$ ($0 \le x \le 1$)

Iwona Szkoda, Paz Vaqueiro, Andrew McDowall, Anthony V. Powell and Clemens Ritter

Page 2806

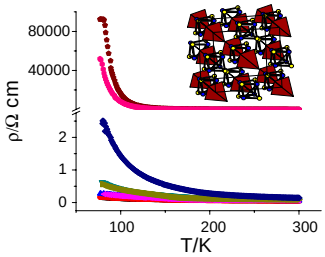

Chemical substitution and sulfur non-stoichiometry produce dramatic changes in the transport properties of defect thiospinels $Ga_{1-x}Ge_xV_4S_{8-\delta}$.

Oxygen vacancy ordering within anion-deficient Ceria

S. Hull, S.T. Norberg, I. Ahmed, S.G. Eriksson, D. Marrocchelli and P.A. Madden

Page 2815

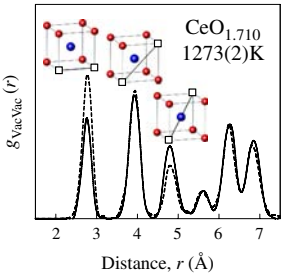

Partial radial distribution function for oxygen vacancies within $CeO_{1.710}$ at 1273 K (solid line) showing the increased tendency for local ordering in ⟨111⟩ directions compared to a random distribution (dashed line).

Mechanism for the formation of tin oxide nanoparticles and nanowires inside the mesopores of SBA-15

G. Satishkumar, L. Titelman and M.V. Landau

Page 2822

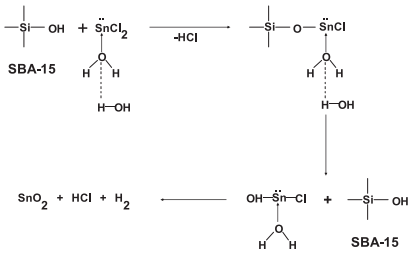

The mechanism of formation of polycrystalline tin oxide nanoparticles (NP) and nanowires was investigated using nanocasting approach included solid–liquid strategy for insertion of $SnCl_2$ precursor and SBA-15 silica as a hard template. It was found that the structure silanols of silica matrix play a vital role in creating the tin oxide NP during thermal treatment.

Flash microwave synthesis and sintering of nanosized $La_{0.75}Sr_{0.25}Cr_{0.93}Ru_{0.07}O_{3-\delta}$ for fuel cell application
L. Combemale, G. Caboche and D. Stuerga
Page 2829

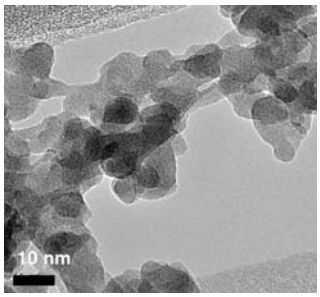

TEM photograph of $La_{0.75}Sr_{0.25}Cr_{0.93}Ru_{0.07}O_{3-\delta}$ obtained by microwave flash synthesis. This picture confirms the nanometric size of the ceramic particles.

The character of W-doped one-dimensional VO_2 (M)
Jing Li, Chun-yan Liu and Li-juan Mao
Page 2835

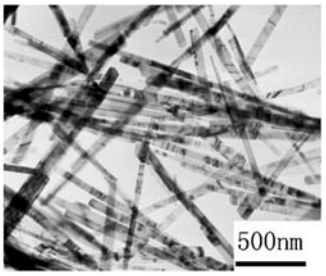

One-dimensional W-doped VO_2 (M) solid solutions with a various doped content were synthesized under hydrothermal condition and subsequent calcination. The physical–chemical and phase transformation character were explored, subsequently.

Lanthanide (III) addition of $[Mo_2O_3S(HNTA)_2]^{2-}$ (*Ln* = Eu, Dy)
Zhen-Hua Dang, Si Mou and Li Xu
Page 2840

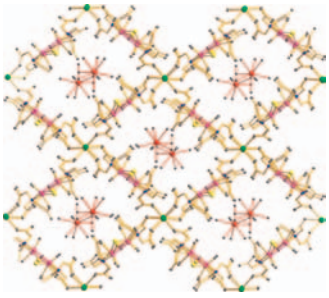

The reactions of $LnCl_3$ and $Na_2[Mo_2O_3S(HNTA)_2]$ result in the 3-D open framework of $Na[Mo_2O_3S(HNTA)_2]_2$ templated by $Eu(H_2O)_9^{3+}$ (**1**) and the pentanuclear heterometallic cluster $Na\{(H_2O)_6Dy[Mo_2O_3S(HNTA)_2]_2\}$ (**2**) as a consequence of lanthanide contraction.

Crystal structure and electron density in the apatite-type ionic conductor $La_{9.71}(Si_{5.81}Mg_{0.18})O_{26.37}$
Roushown Ali, Masatomo Yashima, Yoshitaka Matsushita, Hideki Yoshioka and Fujio Izumi
Page 2846

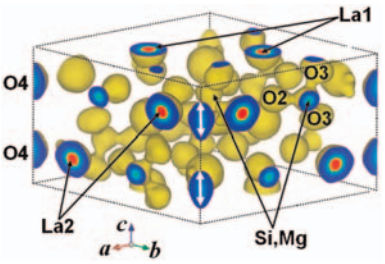

Equielectron density surfaces at 1.0 $Å^{-3}$ of apatite-type $La_{9.71}(Si_{5.81}Mg_{0.18})O_{26.37}$ at 302 K. O4 atoms have large distribution along the $\langle 001 \rangle$ direction (white arrows).

Syntheses, crystal structures, and water adsorption behaviors of jungle-gym-type porous coordination polymers containing nitro moieties
Kazuhiro Uemura, Fumiaki Onishi, Yukari Yamasaki and Hidetoshi Kita
Page 2852

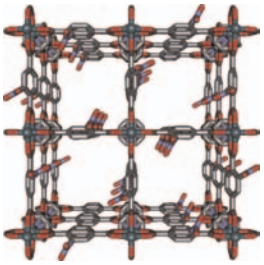

Two hydrophilic porous coordination polymers, $[Zn_2(bdc\text{-}NO_2)_2(dabco)]_n$ (**2**, bdc-NO_2 = nitroterephthalate, dabco = 1,4-diazabicyclo[2.2.2]octane) and $[Zn_2(bdc\text{-}(NO_2)_2)_2(dabco)]_n$ (**3**, bdc-$(NO_2)_2$ = 2,5-dinitroterephthalate), have been synthesized and characterized by single X-ray analyses, thermal gravimetry, and adsorption measurements.

Structural characterisation of the perovskite series $Sr_xCa_{1-x-y}Nd_yMnO_3$: Influence of the Jahn–Teller effect
Brendan J. Kennedy, Paul J. Saines, Jimmy Ting, Qingdi Zhou and Justin A. Kimpton
Page 2858

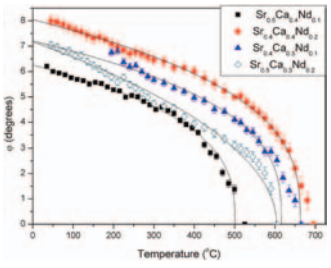

Structural studies of oxides of the type $Sr_xCa_{1-x-y}Nd_yMnO_3$ series illustrate the continuous removal of the octahedral tilting, despite the loss of orbital ordering.

Continued

Utilization of iron oxide film obtained by CVD process as catalyst to carbon nanotubes growth
Mariane C. Schnitzler and Aldo J.G. Zarbin
Page 2867

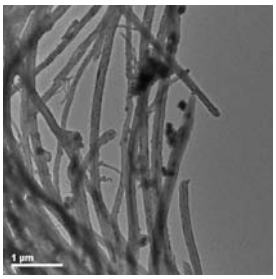

Thin films of Fe_2O_3 were obtained on silica glass substrates through the thermal decomposition of ferrocene in air, and subsequently used as catalyst on the growth of carbon nanotubes.

Synthesis and magnetic properties of 12L-perovskites $Ba_4LnIr_3O_{12}$ (Ln = lanthanides)
Yuki Shimoda, Yoshihiro Doi, Makoto Wakeshima and Yukio Hinatsu
Page 2873

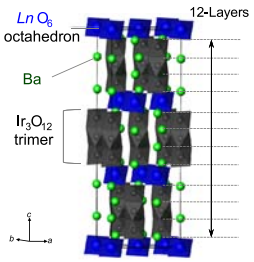

New quadruple perovskite oxides $Ba_4LnIr_3O_{12}$ were prepared and they form the perovskite-type structure with 12 layers, in which Ir_3O_{12} trimers and LnO_6 octahedra are alternately linked by corner-sharing. For Ln = Ce, Pr, and Tb compounds, an antiferromagnetic transition was observed at 10.5, 35, and 16 K, respectively.

Structural, mechanical, and electronic properties of TaB_2, TaB, IrB_2, and IrB: First-principle calculations
Wen Jie Zhao and Yuan Xu Wang
Page 2880

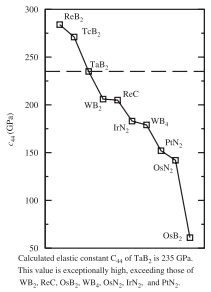

Elastic constant c_{44} of TaB_2 is calculated to be 235 GPa. This value is exceptionally high, exceeding those of WB_2, OsB_2, WB_4, OsN_2, IrN_2, and PtN_2.

Epitaxial growth of high purity cubic InN films on MgO substrates using HfN buffer layers by pulsed laser deposition
R. Ohba, J. Ohta, K. Shimomoto, T. Fujii, K. Okamoto, A. Aoyama, T. Nakano, A. Kobayashi, H. Fujioka and M. Oshima
Page 2887

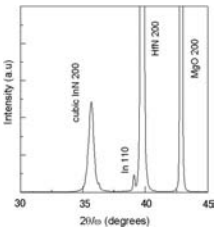

Cubic InN films have been grown on MgO substrates with HfN buffer layers by pulsed laser deposition (PLD). It has been revealed that the phase purity of the cubic InN films was as high as 99 %, which can be attributed to the use of HfN buffer layers and the enhanced surface migration of the film precursors by the use of PLD.

Crystal structure and hydrogenation properties of pseudo-binary $Mg_6Pd_{0.5}Ni_{0.5}$ complex metallic alloy
F. Cuevas, J.F. Fernández, J.R. Ares, F. Leardini and M. Latroche
Page 2890

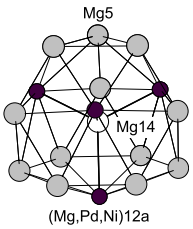

Coordination polyhedron around site Mg14 in pseudobinary Mg_6(Pd,Ni) compounds.

Syntheses, crystal structures and Raman spectra of $Ba(BF_4)(PF_6)$, $Ba(BF_4)(AsF_6)$ and $Ba_2(BF_4)_2(AsF_6)(H_3F_4)$; the first examples of metal salts containing simultaneously tetrahedral BF_4^- and octahedral AF_6^- anions
Matic Lozinšek, Tina Bunič, Evgeny Goreshnik, Anton Meden, Melita Tramšek, Gašper Tavčar and Boris Žemva
Page 2897

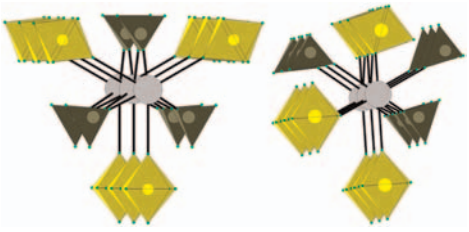

The first three compounds, containing simultaneously tetrahedral BF_4^- and octahedral AF_6^- (A = P, As) anions have been synthesized and characterized by Raman spectroscopy and X-ray single crystal diffraction. In the system $BaF_2/BF_3/PF_5$/anhydrous hydrogen fluoride (aHF) the compound $Ba(BF_4)(PF_6)$ was isolated. In the analogous system with AsF_5 instead of PF_5 the compound $Ba(BF_4)(AsF_6)$ was obtained. When the system $BaF_2/BF_3/AsF_5$/aHF is made basic with an extra addition of BaF_2, the compound $Ba_2(BF_4)_2(AsF_6)(H_3F_4)$ was prepared.

Locating redox couples in the layered sulfides with application to $Cu[Cr_2]S_4$
John B. Goodenough and Youngsik Kim
Page 2904

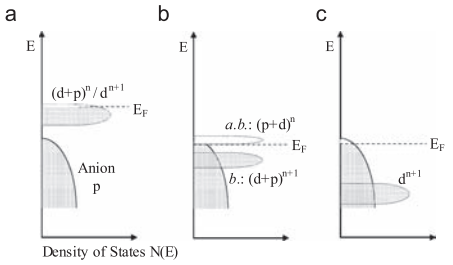

Schematic representation of a slightly oxidized redox couple as it passes through the top of the anion-*p* bands: (a) itinerant versus polaronic character of hole states of couple on the approach to the top of anion-*p* band, (b) pinned couple with predominantly antibonding (*a.b.*) anion-*p* hole states and predominantly cation-*d* bonding (*b.*) states, (c) couple too far below top of anion-*p* band for significant cation-*d* character in hole states.

One-pot, high-yield synthesis of titanate nanotube bundles decorated by Pd (Au) clusters for stable electrooxidation of methanol
Xiudong Xue, Li Gu, Xuebo Cao, Yingying Song, Lianwen Zhu and Peng Chen
Page 2912

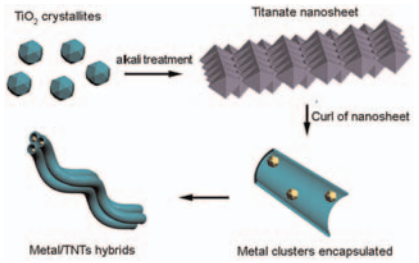

Titanate/Au and titanate/Pd nanotube bundles have been fabricated by taking advantage of the unique scrolling growth mechanism of titanate tubes. The titanate/Pd hybrids show stable catalytic effects toward the electrooxidation of methanol.

Metal–organic coordination architectures of azole heterocycle ligands bearing acetic acid groups: Synthesis, structure and magnetic properties
Bo-Wen Hu, Jiong-Peng Zhao, Qian Yang, Tong-Liang Hu, Wen-Ping Du and Xian-He Bu
Page 2918

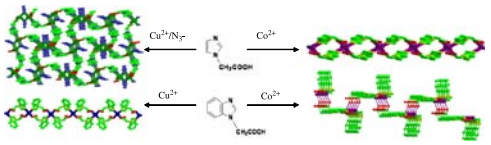

The synthesis, crystal structure, and magnetic properties of the new coordination complexes with azole heterocycle ligands bearing acetic acid groups are reported.

Investigation of substitution effects and the phase transition in type-I clathrates $Rb_xCs_{8-x}Sn_{44}\square_2$ ($1.3 \le x \le 2.1$) using single-crystal X-ray diffraction, Raman spectroscopy, heat capacity and electrical resistivity measurements
Andreas Kaltzoglou, Thomas F. Fässler, Christian Gold, Ernst-Wilhelm Scheidt, Wolfgang Scherer, Tetsuji Kume and Hiroyasu Shimizu
Page 2924

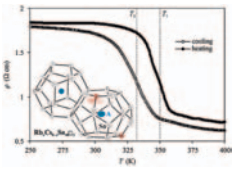

The effects of substitution of cations in the type-I clathrates $Rb_xCs_{8-x}Sn_{44}$ ($1.3 \le x \le 2.1$) are reported. The distribution of the guests in the Sn cages under different reaction stoichiometries and annealing times is studied by X-ray diffraction. A structural phase transition in $Rb_{1.4}Cs_{6.6}Sn_{44}$ at 333–363 K affects significantly the electrical resistivity and heat capacity.

Giant dielectric constant response of the composites in ternary system $CuO–TiO_2–CaO$
Michael Veith, Shuhua Ren, Matthias Wittmar and Henning Bolz
Page 2930

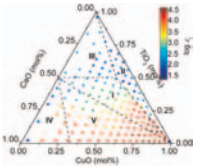

In the ternary system, $CuO–TiO_2–CaO$, a giant dielectric constant (ε_r) above 10^4 (red color) was observed in most of the composites sintered at only 950 °C in the CuO-rich region. Dashed lines show the phase boundaries.

Rapid Communications

Effects of substrate temperature on properties of ITO–ZnO composition spread films fabricated by combinatorial RF magnetron sputtering
Gi-Seok Heo, In-Gi Gim, Jong-Woon Park, Kwang-Young Kim and Tae-Won Kim
Page 2937

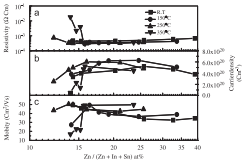

The effects of substrate temperature on properties of ITO–ZnO films were investigated by using combinatorial RF magnetron sputtering. The amorphous ITO–ZnO film had lower resistivity than polycrystalline films. The minimum resistivity of $3.0 \times 10^{-4}\,\Omega$ cm was obtained with the substrate temperature of 250 °C and the zinc contents of 16.0 at%. The electronic states of ITO–ZnO films were discussed with related to the formation of transparent amorphous oxide semiconductor (TAOS).

Continued

Synthesis of uniform CdS nanowires in high yield and its single nanowire electrical property
Shancheng Yan, Litao Sun, Peng Qu, Ninping Huang, Yinchen Song and Zhongdang Xiao
Page 2941

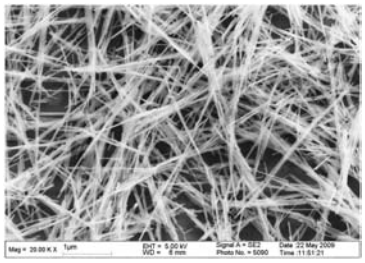

Large-scale high quality CdS nanowires (NWs) with uniform diameter were synthesized by using a rapid and simple solvothermal route. The reaction time is reduced to 2 h, comparing to other synthesis which needed long reaction time up to 12 h. In addition, the as-prepared CdS nanowires have more uniform diameter and high yield. More importantly, the *I–V* curve of present single CdS nanowire has a good symmetric characteristic as expected by the theory.

Corrigendums

Corrigendum to: "High-pressure structural behavior and equation of state of $NaZnF_3$" [Journal of Solid State Chemistry 182 (2009) 1545–1549]
Sergey Yakovlev, Maxim Avdeev, Eran Sterer, Yaron Greenberg and Mohamed Mezouar
Page 2946

Corrigendum to "Synthesis, crystal structure and characterization of iron pyroborate ($Fe_2B_2O_5$) single crystals" [J. Solid State Chem. 182 (2009) 2004–2009]
Tetsuya Kawano, Haruhiko Morito, Takahiro Yamada, Takeyoshi Onuma, Shigefusa F. Chichibu and Hisanori Yamane
Page 2947